

**Noncollinear nature of the magnetic ground states in an fcc  $[\text{Fe}_7|\text{Cu}_7]_n$  superlattice**Xinzhe He<sup>1</sup>, Cunxu Gao,<sup>2</sup> and Lei Wang<sup>1,\*</sup><sup>1</sup>*Center for Spintronics and Quantum Systems, State Key Laboratory for Mechanical Behavior of Materials, Xi'an Jiaotong University, No. 28 Xianning West Road Xi'an, Shaanxi 710049, China*<sup>2</sup>*Key Laboratory for Magnetism and Magnetic Materials of the Ministry of Education, Lanzhou University, Lanzhou 730000, China*

(Received 4 January 2023; accepted 9 August 2023; published 18 August 2023)

Due to its complex magnetic structure, fcc Fe grown on a Cu(100) substrate has been studied for decades. Many experimental measurements have gradually confirmed that fcc Fe|Cu(100) films have a noncollinear magnetic configuration. In contrast, current theoretical calculations have found that collinear magnetic configurations are always more stable than noncollinear magnetic configurations. To clarify this discrepancy, we set up Fe|Cu(100) films and  $[\text{Fe}_7|\text{Cu}_7]_n$  superlattice and carry out first-principles calculations to study the magnetic ground states therein. We find that the exchange interactions along the normal direction of the thin film exhibit long-range RKKY-like behavior. Using these exchange interactions, we construct an effective Hamiltonian, with which the noncollinear magnetic ground states were found. Moreover, Monte Carlo simulations confirm these noncollinear magnetic ground states to be stable at a finite temperature. Thus, our results catch the physical origin of the noncollinear magnetic ground states in fcc Fe-based films and reveal that even the collinear exchange coupling may induce noncollinear magnetic states.

DOI: [10.1103/PhysRevB.108.064424](https://doi.org/10.1103/PhysRevB.108.064424)**I. INTRODUCTION**

While bulk fcc Fe is known to be a high-temperature phase above 1200 K, it can be stabilized below room temperature by epitaxial growth on fcc Cu(100) substrates, which is promising for broader applications. Thus, a large number of experiments [1–17] and theoretical calculations [18–32] have been carried out to study Fe|Cu(100) films, including their sample preparation, growth mechanism, magnetic properties, crystal structure, etc. For the crystal/magnetic structures of Fe|Cu(100) films, the following consensus has gradually been immersed (there are three kinds of crystal/magnetic structures as a function of the film thickness) [32]: for the film with less than four Fe atomic layers (ALs), the magnetic configuration keeps ferromagnetic (FM); for the film with more than 10 Fe ALs, the crystal structure of film become bcc type and the magnetic structure changes to FM with in-plane easy axes. The most interesting part is the film with the number of Fe layers between five and nine ALs, where the crystal structure of the film is fcc type and the magnetic configurations are richer than expected.

The magnetic configuration of such films was first assumed to be ferromagnetic at the surface with antiferromagnetic ordering in between domains [1,2,19]. However, Amemiya *et al.* [3] and Qian *et al.* [4] both believed that the magnetic texture in Fe|Cu(100) films should be a spin-density wave. Subsequently, a new magnetic configuration was proposed using soft-x-ray resonant magnetic scattering measurements combined with theoretical calculations [5], which is constructed by different blocks with internal robust magnetic configurations, and the magnetic couplings between these

blocks are so weak that it is easy to form noncollinear magnetic configurations. Although there are still disharmonious opinions regarding the details of the magnetic structure, the noncollinear nature of these films has been approved by different groups [3–5,14,17].

However, for theoretical calculations of magnetic configurations of Fe|Cu(100) films, despite the differences in methods and models used by Asada [20], Spisak *et al.* [18], and Zhou *et al.* [33], these results all show that the collinear bilayer antiferromagnetic (CBAFM) configuration tends to be energetically preferred. Furthermore, Yavorsky *et al.* [21] and Spisak *et al.* [23] have proposed that the magnetic configurations therein should be a spin density wave; and Sandratskii [22] claimed that the calculated noncollinear magnetic configurations induced by different blocks are consistent with the experimental results [5]. However, it should be noticed that all the total energies of the above noncollinear results are larger than the CBAFM configurations and they try to attribute the noncollinear magnetic configurations to the energy disturbance by concrete defect patterns or lattice distortions in the films.

To clarify these discrepancies between experimental and theoretical works, in this paper, we report on the first-principle study of the magnetic ground states of fcc Fe-based films. As the  $[\text{Fe}|\text{Cu}]_n$  superlattice has been recently proven to be reliable in experiments with high quality [34], it becomes a promising object to study the corresponding interface effect between Cu and Fe without introducing surface defects and reconstruction. Thus, we mainly set up an  $[\text{Fe}_7|\text{Cu}_7]_n$  superlattice to calculate the exchange interactions based on first-principle calculations, where the subscript “7” stands for 7 ALs in a repetitive structure and “ $n$ ” represents the infinite repeating units with periodic boundary conditions. And to demonstrate the interface is crucial rather than the

\*wanglei.icer@xjtu.edu.cn

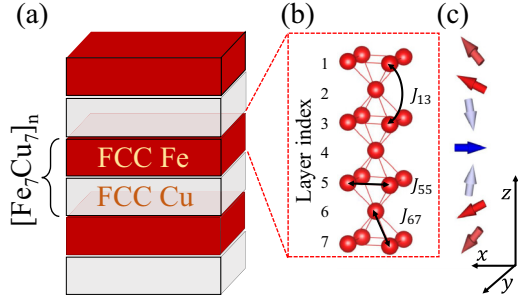


FIG. 1. (a) A sketch of the  $[\text{Fe}_7|\text{Cu}_7]_n$  superlattice. (b) The corresponding ball-stick models of the smallest unit cell with a  $45^\circ$  in-plane rotation to make one effective atom in one layer.  $J_{ij}$ s are the Heisenberg exchange constants between the  $i$ th and  $j$ th layers, accordingly. (c) The noncollinear spin texture of the  $[\text{Fe}_7|\text{Cu}_7]_n$  superlattice

periodic boundary condition from the superlattice, an  $\text{Fe}_7|\text{Cu}_7$  bilayer is also used to calculate the exchange interactions for comparison.

Our results show that the Ruderman-Kittel-Kasuya-Yosida (RKKY)-like [35–38] exchange interaction is observed along the normal direction of both  $[\text{Fe}_7|\text{Cu}_7]_n$  superlattice and  $\text{Fe}_7|\text{Cu}_7$  bilayer, which is demonstrated to come from the intervention of the electrons from Cu around the interfaces. Accordingly, the next-nearest-neighbor coupling dominates, indicating a strong antiferromagnetic coupling therein. Moreover, we construct an effective Hamiltonian using these exchange interactions as well as the magnetic anisotropy energy (MAE) and obtain a series of noncollinear magnetic configurations, which are notably more stable than the CBAFM configuration. To confirm the physical existence of these noncollinear states, Monte Carlo (MC) simulations are carried out at low temperatures. The results reveal that these noncollinear states all converge to a group of similar textures, as shown in Fig. 1(c), where the angles between every two spins are fixed and the texture can be freely rotated. Moreover, the influence of the number of Fe ALs is discussed, where similar noncollinear magnetic ground states are founded with odd Fe ALs while the collinear magnetic ground states are founded with even Fe ALs.

## II. MODEL AND METHOD

The model used in this paper is shown in Figs. 1(a) and 1(b), where the corresponding lattice constants are set to  $3.612 \text{ \AA}$ , and the Fe atoms in the same AL of the superlattice are marked as  $\text{Fe}_{i,i \in \{1 \sim 7\}}$ , with  $i$  representing the layer index. The corresponding effective Hamiltonian of a unit cell can be expressed as  $H = -\sum_{i,j} J_{ij} \vec{S}_i \cdot \vec{S}_j$ , where  $i$  and  $j$  represent the index of Fe atoms,  $J_{ij}$  describes the Heisenberg exchange constants between the  $i$ th atom and  $j$ th atom, and the magnetic vector  $|\vec{S}| = 1$  for generality. In a typical case, to obtain the Heisenberg exchange constants between two different atoms ( $\text{Fe}_k$  and  $\text{Fe}_l$ ), a four-state method [39] is used, in which the total energy can be rewritten as

$$E_{\text{tot}} = E_0 - NJ_{kl} \vec{S}_k \cdot \vec{S}_l - \vec{A}_k \cdot \vec{S}_k - \vec{A}_l \cdot \vec{S}_l \quad (1)$$

where  $E_0$  contains the energies of the nonmagnetic part and the coupling independent of  $\text{Fe}_k$  and  $\text{Fe}_l$ ,  $N$  is the number of

neighboring atoms, and  $\vec{A}_k = \sum_{j \neq l} J_{kj} \vec{S}_j$ ,  $\vec{A}_l = \sum_{j \neq k} J_{lj} \vec{S}_j$ , representing the effective field on  $\text{Fe}_k$  and  $\text{Fe}_l$ , respectively. Then, if we have the energies of four different magnetic states between  $\text{Fe}_k$  and  $\text{Fe}_l$  ( $a : \uparrow\uparrow$ ,  $b : \uparrow\downarrow$ ,  $c : \downarrow\uparrow$ ,  $d : \downarrow\downarrow$ ), then the corresponding Heisenberg exchange constant will be  $J_{kl} = (E_b + E_c - E_a - E_d)/4N$ , with  $E_{a,b,\dots}$  being the energies of different magnetic configurations. Notably, all calculations are independent of the spin texture of the other Fe atoms except  $\text{Fe}_k$  and  $\text{Fe}_l$ , and we set them all parallel to the  $+z$  axis for simplicity. Moreover, there is a spatial inverse symmetry in the  $[\text{Fe}_7|\text{Cu}_7]_n$  superlattice; thus, the Heisenberg exchange constants follow the relationship of  $J_{i,j} = J_{8-i,8-j}$ , which can simplify our calculations.

It is efficient and convenient to calculate the above total energies  $E_{a,b,\dots}$  by density functional theory, which can be realized by the Vienna *ab initio* simulation package (VASP) [40,41]. Here, all calculations are carried out with the generalized gradient approximation (GGA) and a plane-wave basis set within the framework of the projector augmented wave (PAW) method [42,43]. The cutoff energy for the basis is 500 eV, and the convergence criterion for the electron density self-consistency cycles is  $10^{-6}$  eV. In the Brillouin zone, we sample  $(13 \times 13 \times 3)$  k-point grids using the Monkhorst-Pack scheme [44] to ensure that the results converge. Additionally, for perpendicular magnetic anisotropy, spin-orbit coupling is included.

## III. RESULTS AND ANALYSIS

We first focus on the in-plane Heisenberg exchange constants  $J_{ii,i \in \{1,7\}}$ , which can be calculated by expanding a  $10 \times 1 \times 1$  supercell of the  $[\text{Fe}_7|\text{Cu}_7]_n$  superlattice, and the results are  $J_{11} = J_{77} = 40.44 \text{ meV}$ ,  $J_{22} = J_{66} = 28.87 \text{ meV}$ ,  $J_{33} = J_{55} = 29.46 \text{ meV}$ , and  $J_{44} = 30.50 \text{ meV}$  for the nearest-neighbor atoms. Meanwhile, for the next-nearest-neighbor atoms, the in-plane Heisenberg exchange constants decay very fast to about  $-1.52 \text{ meV}$ ,  $-0.0116 \text{ meV}$ ,  $1.16 \text{ meV}$ ,  $1.40 \text{ meV}$ ,  $1.16 \text{ meV}$ ,  $-0.0116 \text{ meV}$ , and  $-1.52 \text{ meV}$  for  $i = 1 \dots 7$ , respectively. It is apparent that the in-plane Heisenberg exchange constants are dominated by the nearest-neighbor atoms and all favor the ferromagnetic states, indicating that the superlattice is a layered spin texture, which can be also demonstrated by the MC simulations as discussed in Fig. 5 below. Therefore, with this information, we now focus on interlayer coupling in the following. The corresponding interlayer Heisenberg exchange constants as a function of distance are plotted in Fig. 2, where the red circles represent  $J_{1i,i \in \{2,7\}}$  and blue squares represent the other Heisenberg exchange constants away from the Fe/Cu interfaces. In addition, we estimate the Heisenberg exchange constants by the total energies of different magnetic configurations from a 5-ALs sample in Ref. [20], and the results are also plotted in Fig. 2 by green triangles for comparison. The calculated  $J_{1i}$ s agree well with the results from Ref. [20], supporting the reliability of our calculations. Moreover, to rule out the influence of the periodical boundary condition in the superlattice, the  $\text{Fe}_7|\text{Cu}_7$  bilayer is constructed with a similar crystal structure, and the corresponding results are plotted in Fig. 2 by magenta circles. It can be seen that the Heisenberg exchange constants of  $\text{Fe}_7|\text{Cu}_7$  bilayer are quite close to that of  $[\text{Fe}_7|\text{Cu}_7]_n$  su-

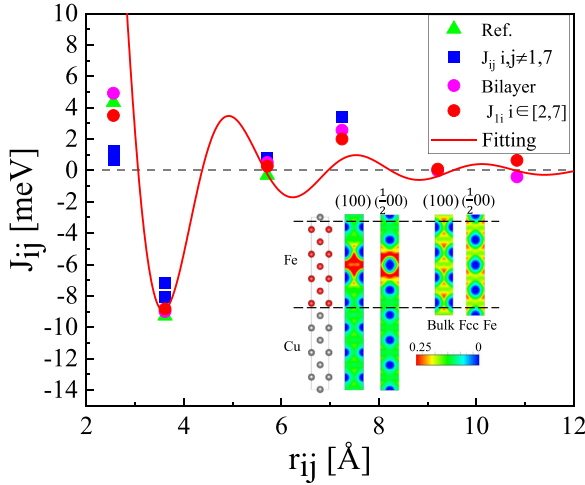


FIG. 2. The interlayer Heisenberg exchange constants  $J_{ij,i \neq j}$  vs the corresponding distance  $r_{ij}$  for  $[\text{Fe}_7|\text{Cu}_7]_n$  superlattice (red circles for  $J_{ij}, i \in [2, 7]$ ; blue squares for  $J_{ij}, i, j \neq 1, 7$ ) and  $\text{Fe}_7|\text{Cu}_7$  bilayer (magenta circles for  $J_{ij}, i \in [2, 7]$ ), respectively. The green triangles are estimated from the total energies in Ref. [20] for comparison. The red solid line represents the fitting results using the RKKY-like equation (2). The inset shows the calculated electron local density for the (100) and  $(\frac{1}{2}00)$  planes of the  $[\text{Fe}_7|\text{Cu}_7]_n$  superlattice and bulk fcc Fe, respectively.

perlattice, indicating that the calculated Heisenberg exchange constants are mainly from a single Fe layer in the superlattice and insensitive to the interaction between Fe layers that separated by Cu layers.

It is notable that the largest Heisenberg exchange constant appears at a distance of  $r_{ij} = 3.612 \text{ \AA}$  for the next-nearest-neighbor atoms instead of the nearest-neighbor atoms with  $r_{ij} = 2.554 \text{ \AA}$ . Moreover, the corresponding sign change between the nearest- and next-nearest-neighbor Heisenberg exchange constants introduces competition in the formation of the magnetic ground states, which may result in complicated spin textures in the  $[\text{Fe}_7|\text{Cu}_7]_n$  superlattice. Furthermore, the oscillated  $J_{ij}$  reminds us of the RKKY interaction, which obeys the rule [35–37]

$$J(r) = J_0 \left( \frac{\cos(2k_F r)}{r^3} - \frac{\sin(2k_F r)}{r^4} \right) \quad (2)$$

with  $k_F$  being the wave vector at the Fermi energy. Therefore, we try to fit our results by the above equation, which is shown by the red solid line in Fig. 2, representing  $J(r) \simeq 417.90 \times (\cos(2.46r)/r^3 - \sin(2.46r)/r^4)$ . It should be noted that the exchange constant between the nearest-neighbor atoms is dominant by the direct Heisenberg exchange interaction [45] and thus, the first point with  $r_{ij} = 2.554 \text{ \AA}$  is neglected in the fitting. Here,  $k_F \simeq 1.23 \text{ \AA}^{-1}$ , which is in the same order of the rare earth materials, such as  $\text{ErB}_4$ ,  $\text{DyB}_4$ ,  $k_F \simeq 1.7 \text{ \AA}^{-1}$  [45],  $\text{TmB}_4$ ,  $k_F \simeq 1.38 \text{ \AA}^{-1}$  [46,47],  $\text{Pr}_2\text{Ir}_2\text{O}_7$ ,  $k_F \simeq 0.50 \text{ \AA}^{-1}$  [48],  $\text{RbEuFe}_4\text{As}_4$ ,  $k_F \simeq 0.60 \text{ \AA}^{-1}$  [49], etc. We also notice that the  $k_F$  in our system is quite close to the free electron model of Cu ( $k_F \simeq 1.36 \text{ \AA}^{-1}$ ), therefore, it could be reasonable to relate the origin of the RKKY interaction to the charge transfer around Fe|Cu interface, which is different from the conventional RKKY interaction in rare-earth materials.

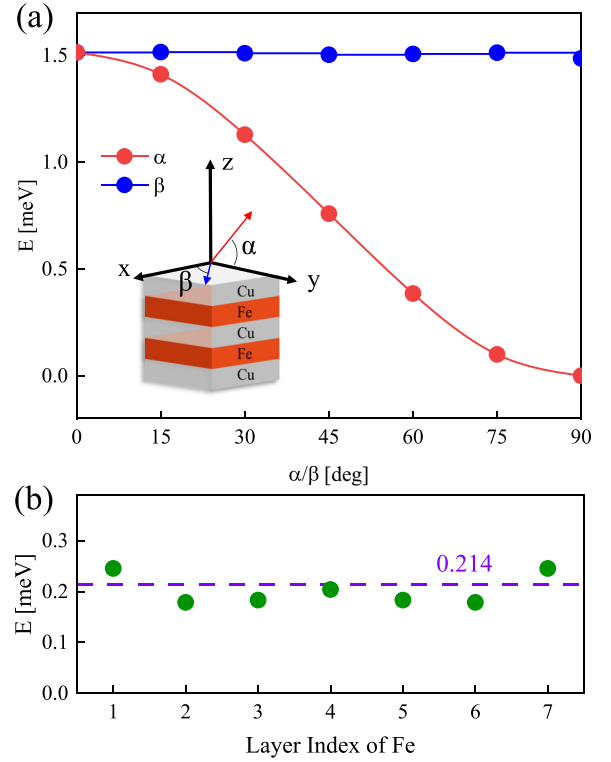


FIG. 3. (a) Normalized total energy vs the direction of magnetization, where  $\alpha/\beta$  stands for the angle between the direction of magnetization and the  $y/x$  axis. The inset shows the global axis in the  $[\text{Fe}_7|\text{Cu}_7]_n$  superlattice with the definition of  $\alpha$  and  $\beta$ . (b) The layer-resolved magnetic anisotropy energy (MAE) from the four-state methods [39] (green circles), and the dashed violet line represents the MAE calculated from the total energies in (a).

On top of the above consideration, the corresponding electron localization function (ELF) [50] is calculated by the equation  $\text{ELF} = (1 + (D/D_0)^2)^{-1}$ , where  $D = \sum_i |\nabla \varphi_i|^2 - (\nabla \rho)^2 / (4\rho)$ ,  $D_0 = \frac{3}{5} (6\pi^2)^{\frac{2}{3}} \rho^{\frac{5}{3}}$ ,  $\varphi_i$  represents the orbital wave function and  $\rho$  stands for the density matrix. The possible values of the ELF are limited in the range of  $[0 \sim 1]$ , with the upper limit 1 corresponding to a totally localized state. The calculated results for the  $[\text{Fe}_7|\text{Cu}_7]_n$  superlattice and bulk fcc Fe are shown in the inset of Fig. 2, respectively. Typically, for simplicity, we only show the ELF on the (100) and  $(\frac{1}{2}00)$  planes for comparison. The ELF of the  $[\text{Fe}_7|\text{Cu}_7]_n$  superlattice around the interfaces are significantly smaller than those of the bulk fcc Fe. According to the rule of the RKKY interaction [35–37], the itinerant electrons (small ELF) will contribute to the indirect coupling between Fe atoms with longer distances, and the RKKY-like interaction in the  $[\text{Fe}_7|\text{Cu}_7]_n$  superlattice should come from the intervention of the  $4s$  electrons of the fcc Cu at the interfaces.

Moreover, to obtain the magnetic ground states of  $[\text{Fe}_7|\text{Cu}_7]_n$ , the MAE is also needed, even though the corresponding spin-orbit coupling may be weak. Figure 3(a) plots the angular dependence of the total energy of the  $[\text{Fe}_7|\text{Cu}_7]_n$  superlattice, where the energy does not change with changing  $\beta$  inside the  $x$ - $y$  plane but shows a cos-like curve as a function of  $\alpha$ , indicating a typical uniaxial magnetic anisotropy along the normal direction ( $z$ ) of the film. In addition, if we

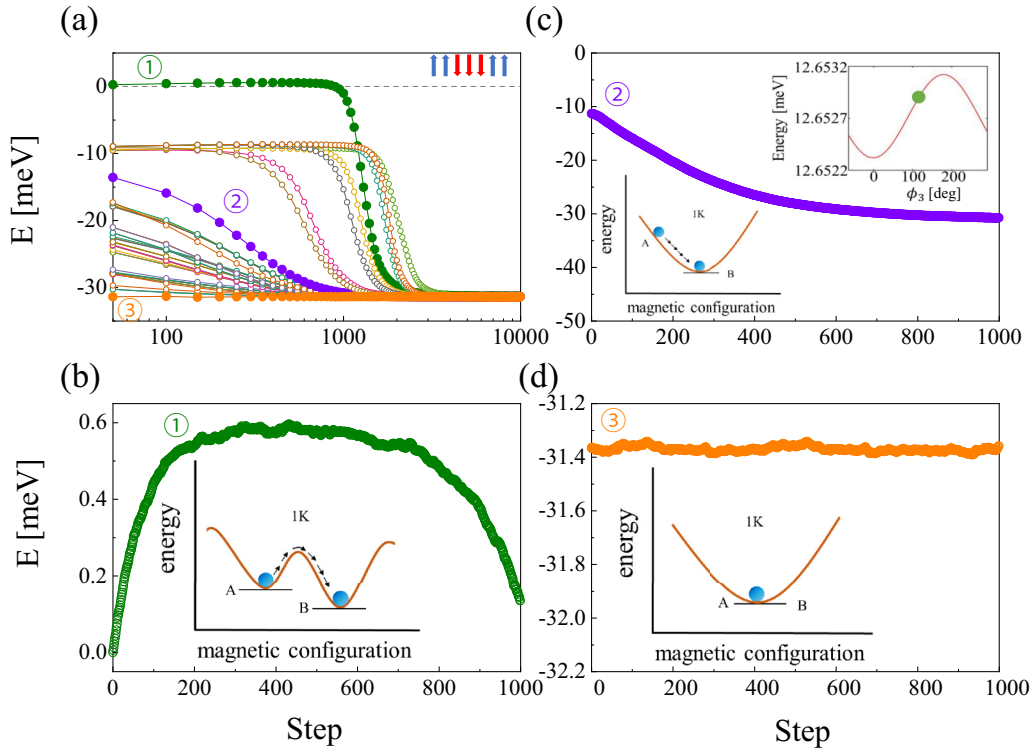


FIG. 4. (a) Evolution of the magnetic configurations obtained from the interior-point algorithm. [(b)–(d)] Details of the first 1000 steps for the corresponding metastable (①), unstable (②), and stable state (③) under MC simulations. Here, all calculations are calculated by the Monte Carlo method at 1 K, and the energies are normalized by the energy of the collinear phase, as shown by the dashed horizontal line in (a). The insets illustrate the change of the states from “A” to “B” in the numerical magnetic configurations with a finite temperature.

divide the MAE into every Fe atom equally, then the atomic magnetic anisotropy energy (aMAE) is estimated as  $K_i = 0.214$  meV/atom. To check the reliability of this assumption, we use a similar four-state method [39] to calculate the aMAE for all Fe atoms in the  $[\text{Fe}_7|\text{Cu}_7]_n$  superlattice, and the results are plotted in Fig. 3(b), with the dashed line representing the aMAE from the total energies. Here, we note that the calculated aMAEs are all around the dashed line; thus, we set  $K_i = 0.214$  meV/atom in the following calculations for simplicity.

In addition to the above considerations, the whole Hamiltonian of the system can be written as

$$H = - \sum_{i,j} J_{ij} \vec{S}_i \cdot \vec{S}_j - \sum_i K_i (\vec{S}_i \cdot \vec{z})^2 \quad (3)$$

where  $K_i$  represents the aMAE of the corresponding Fe $_i$  and  $\vec{S}_i = (\sin \theta_i \cos \phi_i, \sin \theta_i \sin \phi_i, \cos \theta_i)$  represents the direction of magnetization of Fe $_i$ , with  $\theta_i$  and  $\phi_i$  representing the polar and azimuth angles in the spherical coordinate system, respectively. In this sense, as  $J_{ij}$  and  $K_i$  are already known from the above calculations, there remain 14 undetermined coefficients ( $\theta_i$  and  $\phi_i$  with  $i \in \{1 \cdots 7\}$ ) in Eq. (3). Moreover, as the total energy is insensitive to  $\beta$ , as shown in Fig. 3(a), the whole spin texture can be rotated freely in the  $x$ - $y$  plane. Therefore, there are only 13 independent parameters, and we fix  $\phi_1 = 0$  to avoid misleading the results.

To find all possible nontrivial magnetic ground states, the interior-point (IP) algorithm is used one million times with random initial directions of every Fe atom to search the

standing points of Eq. (3). After the simulations, we find 97 typical magnetic configurations from the standing points in total, and the energies of these 97 different magnetic configurations are all smaller than that of the collinear antiferromagnetic configuration ( $\uparrow\uparrow\downarrow\downarrow\uparrow\uparrow$ ), as shown in Fig. 4. However, the mathematical solver may generate unphysical results. Thus, we use these 97 magnetic configurations as the initial states and carry out Monte Carlo (MC) calculations at 1 K to check whether these states can exist at finite temperature. Technically, the MC calculations are realized by an open source code UppASD [51,52], in which we set up a  $25 \times 25 \times 1$  supercell with the calculated  $J_{ij}$  and  $K_i$  from Fig. 2 and Fig. 3 to construct the Hamiltonian and use the semi-implicit midpoint solver with a time step of  $\tau = 10^{-16}$  s and a typical damping parameter 0.1 for the time-dependent evolutions.

As shown in Fig. 4(a), after a sufficient number of iterations, all 97 magnetic configurations obtained by the IP algorithm converge to a similar energy level, indicating that most of the 97 magnetic configurations are not stable at a finite temperature. For a clear view of the simulations, Figs. 4(b)–4(d) show the details of the first 1000 steps of the MC simulation for three typical states, respectively. Accordingly, Fig. 4 displays a metastable magnetic state obtained from the numerical algorithms, in which the system goes through a small energy barrier and converges to the ground state; Fig. 4(c) corresponds to the unstable magnetic state. To figure out its origin, the energy versus  $\phi_3$  from Eq. (3) with fixing all other parameters are plotted in the inset of Fig. 4(c),

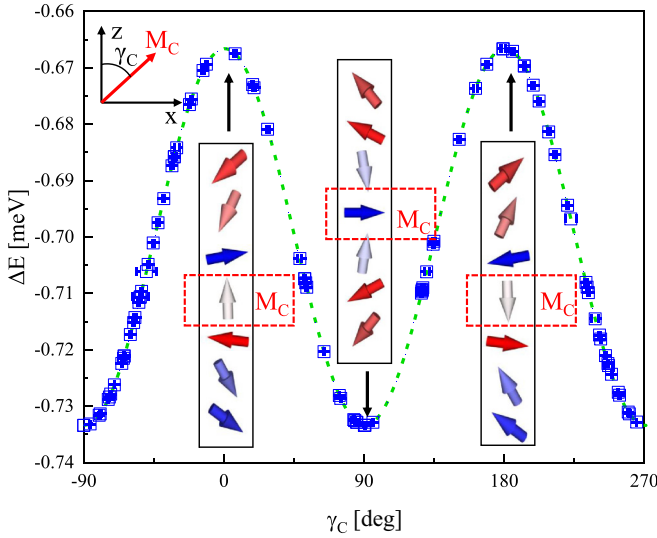


FIG. 5. The normalized energies vs the spin textures (blue squares) of all magnetic configurations obtained from Fig. 4 after evolution at 1 K. Here,  $M_C$  represents the direction of the magnetization of the central Fe atom in the  $[\text{Fe}_7|\text{Cu}_7]_n$  superlattice,  $\gamma_C$  stands for the angle between the  $M_C$  and  $z$  axes, and all relative angles between every two Fe atoms are fixed. The dashed green line is from Eq. (4) analytically, and the insets show the spin textures of the corresponding states.

and the green circle displays the initial state obtained by the IP algorithm. It can be seen that this state is not stable but varies inside a small energy window ( $10^{-3}$  meV), which deceives the IP algorithm; Fig. 4(d) covers most of the results and represents the magnetic ground state of the system, which is quite stable and remains unchanged in the MC simulation at finite temperature.

Moreover, even though the converged energies after MC simulation in Fig. 4 are close to each other, the detailed values of  $\theta_i$  and  $\phi_i$  are very different when we go deep into the directions of the magnetization of the corresponding  $\text{Fe}_i$  atoms from the MC simulations. Furthermore, we also note that the relative angles between any  $\text{Fe}_i$  and  $\text{Fe}_j$  are approximately the same for all 97 magnetic configurations after the MC simulations and that the magnetizations are all in the same plane. Thus, we define the direction of the central Fe atom ( $\text{Fe}_4$ ) as  $M_C$ , the angle between  $M_C$  and  $z$  axis as  $\gamma_C$ , and fix the angles between any two spins inside the  $[\text{Fe}_7|\text{Cu}_7]_n$  superlattice, as shown in the insets of Fig. 5. Then, we have the relation between  $\gamma_C$  and the converged energies from the final step of Fig. 4 and plot them in Fig. 5 by blue squares.

The curve in Fig. 5 shows a cos-like shape, reminding us of the MAE term in Eq. (3), which can be rewritten as  $\Delta E = -\sum_i K_i \cos^2 \theta_i$ . Because the angles between the magnetization directions of  $\text{Fe}_i$  and  $\text{Fe}_j$  are fixed, as discussed above, we also define a series of constants  $\Delta\gamma_i \equiv \theta_i - \gamma_C$  to describe the angles between  $\text{Fe}_i$  and  $M_C$ . Thus, we have the normalized MAE as

$$\Delta E = -\sum_i K_i \cos^2 (\gamma_C + \Delta\gamma_i). \quad (4)$$

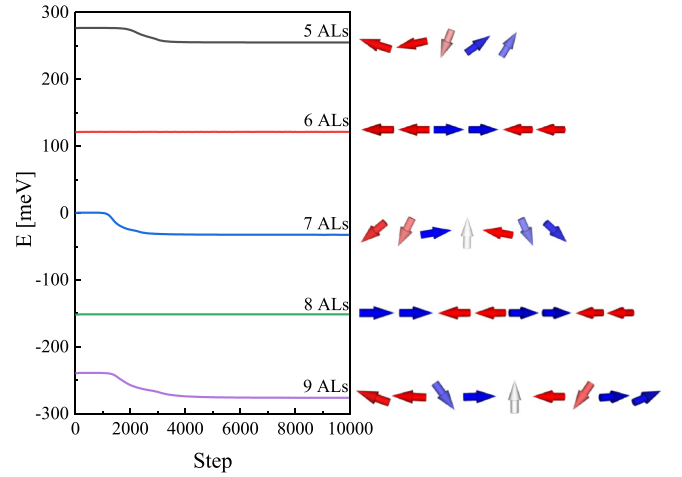


FIG. 6. The evolution of the magnetic configurations for  $[\text{Fe}|\text{Cu}]_n$  superlattice with different Fe ALs. Here the energies are all normalized by the initial energy of  $[\text{Fe}_7|\text{Cu}_7]_n$  and the arrows show the spin textures of the corresponding magnetic ground states.

By submitting  $K_i = 0.214$  meV/atom, the analytical MAE as a function of  $\gamma_C$  can be obtained, and the results are plotted in Fig. 5 by the green dashed line.

It can be seen that the converged energies of all 97 magnetic configurations from MC simulations agree well with those from Eq. (4). Therefore, we can conclude that the spin textures are fixed, as shown in the insets of Fig. 5, due to the strong Heisenberg exchange constants, and the competition between temperature and MAE makes the energies of the MC results fluctuate in a small range and the whole spin texture rotate in the  $x$ - $z$  plane. Therefore, the two noncollinear magnetic ground states of the  $[\text{Fe}_7|\text{Cu}_7]_n$  superlattice appear at  $\gamma_C = 90^\circ$  and  $\gamma_C = -90^\circ$ . Notably, because the  $[\text{Fe}_7|\text{Cu}_7]_n$  superlattice is a uniaxial magnetic anisotropic material and has a spatial inverse symmetry, the corresponding spin texture of the magnetic ground states can be rotated freely in the  $x$ - $y$  plane and spatially inverted according to the coordinates of  $\text{Fe}_4$ .

The number of the Fe ALs is also an important issue of the magnetic ground states of the fcc  $\text{Fe}|\text{Cu}$  films, thus we try to analyze the magnetic ground state with 5–9 Fe ALs using a similar method. As shown in Fig. 2, the Heisenberg exchange constants  $J_{ij}$  are close to each other for the same distance  $r_{ij}$  except for that around the  $\text{Fe}|\text{Cu}$  interfaces ( $J_{12}$  and  $J_{67}$  for  $[\text{Fe}_7|\text{Cu}_7]_n$ ). Therefore, it is convenient to construct the total Hamiltonian with  $L$  Fe ALs by fixing the interface Heisenberg exchange constants ( $J_{12} = J_{L,L-1} \simeq 3.5$  meV, and  $J_{11} = J_{LL} \simeq 40.44$  meV) and extending the bulk Heisenberg exchange constants ( $J_{i,i+1,i \neq 1} \simeq 1.27$  meV,  $J_{i,i+2} \simeq -8.83$  meV, and  $J_{ii,i \neq 1} \simeq 30.50$  meV). Then, after MC simulation, their magnetic ground states can be obtained as shown in Fig. 6, together with the corresponding sketch of the spin textures. It can be seen that similar noncollinear magnetic ground states are founded with odd Fe ALs while the collinear magnetic ground states are founded with even Fe ALs, accordingly. These results can be understood by the competition of the following two aspects: (1) the strong FM coupling around the  $\text{Fe}|\text{Cu}$  interface ( $J_{12}$  and  $J_{L,L-1}$ ) leads to parallel order of the corresponding magnetizations and (2) the

AFM coupling for the next nearest-neighbor Fe atoms ( $J_{i,i+2}$ ) favors an antiparallel order in contrary. Thus, for even Fe ALs, the CBAFM configuration satisfies both of the above two conditions, but for odd Fe ALs, these two conditions cannot be satisfied at the same time, and then their competition results in the noncollinear magnetic ground states, as shown in Fig. 6, accordingly. Moreover, in the experiments, it is easy to mix atoms around the interfaces in the thin film growth process. Therefore, there will be both odd and even Fe ALs in a given Fe|Cu thin film in the disorder region. Considering that the CBAFM from even Fe ALs only gives a finite magnetization background, the mixing of the odd and even Fe ALs in experiments should mainly show the noncollinear features.

#### IV. CONCLUSIONS

In summary, we calculate the Heisenberg exchange constants of the  $[\text{Fe}_7|\text{Cu}_7]_n$  superlattice by first-principles calculations. The Heisenberg exchange constants therein show

RKKY-like behavior, which is demonstrated to come from the intervention of the  $4s$  electrons of fcc Cu at the interfaces. Moreover, by constructing an effective Hamiltonian based on the calculated Heisenberg exchange constants and MAE, non-collinear magnetic ground states are found, which originate from the competition between the ferromagnetic coupling in nearest-neighbor atoms and the antiferromagnetic coupling in the next-nearest-neighbor atoms. In addition, MC calculations are carried out to confirm the physical meaning of the observation at a finite temperature.

#### ACKNOWLEDGMENTS

This work was financially supported by the National Key R&D Program of China (Grant No. 2021YFA1202200) and China Postdoctoral Science Foundation (Grant No. 2021T140549). C.G. is supported by the National Natural Science Foundation of China (Grant No. 12074157).

- 
- [1] D. Li, M. Freitag, J. Pearson, Z. Q. Qiu, and S. D. Bader, *Phys. Rev. Lett.* **72**, 3112 (1994).
  - [2] J. Thomassen, F. May, B. Feldmann, M. Wuttig, and H. Ibach, *Phys. Rev. Lett.* **69**, 3831 (1992).
  - [3] K. Amemiya, S. Kitagawa, D. Matsumura, T. Yokoyama, and T. Ohta, *J. Phys.: Condens. Matter* **15**, S561 (2003).
  - [4] D. Qian, X. F. Jin, J. Barthel, M. Klaua, and J. Kirschner, *Phys. Rev. Lett.* **87**, 227204 (2001).
  - [5] H. L. Meyerheim, J.-M. Tonnerre, L. Sandratskii, H. C. N. Tolentino, M. Przybylski, Y. Gabi, F. Yildiz, X. L. Fu, E. Bontempi, S. Grenier, and J. Kirschner, *Phys. Rev. Lett.* **103**, 267202 (2009).
  - [6] K. Heinz, S. Müller, and P. Bayer, *Surf. Sci.* **337**, 215 (1995).
  - [7] H. Jenniches, J. Shen, C. V. Mohan, S. S. Manoharan, J. Barthel, P. Ohresser, M. Klaua, and J. Kirschner, *Phys. Rev. B* **59**, 1196 (1999).
  - [8] M. Weinelt, S. Schwarz, H. Baier, S. Müller, L. Hammer, K. Heinz, and T. Fauster, *Phys. Rev. B* **63**, 205413 (2001).
  - [9] K. Amemiya, D. Matsumura, H. Abe, S. Kitagawa, T. Yokoyama, and T. Ohta, *J. Electron Spectrosc. Relat. Phenom.* **144-147**, 689 (2005).
  - [10] H. L. Meyerheim, R. Popescu, D. Sander, J. Kirschner, O. Robach, and S. Ferrer, *Phys. Rev. B* **71**, 035409 (2005).
  - [11] R. Vollmer, S. van Dijken, M. Schleberger, and J. Kirschner, *Phys. Rev. B* **61**, 1303 (2000).
  - [12] A. Paul, *J. Magn. Magn. Mater.* **505**, 166701 (2020).
  - [13] H. Abe, M. Sakamaki, and K. Amemiya, *J. Phys. Soc. Jpn.* **83**, 084603 (2014).
  - [14] C. E. ViolBarbosa, H. L. Meyerheim, E. Jal, J.-M. Tonnerre, M. Przybylski, L. M. Sandratskii, F. Yildiz, U. Staub, and J. Kirschner, *Phys. Rev. B* **85**, 184414 (2012).
  - [15] A. Biedermann, *Phys. Rev. B* **80**, 235403 (2009).
  - [16] T. Miyamachi, S. Nakashima, S. Kim, N. Kawamura, Y. Tatetsu, Y. Gohda, S. Tsuneyuki, and F. Komori, *Phys. Rev. B* **94**, 045439 (2016).
  - [17] J. Rajeswari, H. Ibach, and C. M. Schneider, *Europhys. Lett.* **101**, 17003 (2013).
  - [18] D. Spišák and J. Hafner, *Phys. Rev. B* **56**, 2646 (1997).
  - [19] R. E. Camley and D. Li, *Phys. Rev. Lett.* **84**, 4709 (2000).
  - [20] T. Asada and S. Blügel, *Phys. Rev. Lett.* **79**, 507 (1997).
  - [21] B. Y. Yavorsky, P. Zahn, and I. Mertig, *Phys. Rev. B* **70**, 014413 (2004).
  - [22] L. M. Sandratskii, *Phys. Rev. B* **81**, 064417 (2010).
  - [23] D. Spišák and J. Hafner, *Phys. Rev. B* **66**, 052417 (2002).
  - [24] T. Kraft, P. M. Marcus, and M. Scheffler, *Phys. Rev. B* **49**, 11511 (1994).
  - [25] R. Lorenz and J. Hafner, *Phys. Rev. B* **54**, 15937 (1996).
  - [26] L. Szunyogh, B. Újfalussy, and P. Weinberger, *Phys. Rev. B* **55**, 14392 (1997).
  - [27] S. S. A. Razee, J. B. Staunton, L. Szunyogh, and B. L. Gyorffy, *Phys. Rev. Lett.* **88**, 147201 (2002).
  - [28] M. Pajda, J. Kudrnovský, I. Turek, V. Drchal, and P. Bruno, *Phys. Rev. Lett.* **85**, 5424 (2000).
  - [29] C. L. Fu and A. J. Freeman, *Phys. Rev. B* **35**, 925 (1987).
  - [30] G. W. Fernando and B. R. Cooper, *Phys. Rev. B* **38**, 3016 (1988).
  - [31] R. Garibay-Alonso, J. Ricardo-Chávez, J. Rodríguez-López, and J. Morán-López, *J. Magn. Magn. Mater.* **514**, 167108 (2020).
  - [32] X. Zhang, T. Hickel, J. Rogal, and J. Neugebauer, *Phys. Rev. Lett.* **118**, 236101 (2017).
  - [33] Y.-m. Zhou, W.-t. Geng, and D.-s. Wang, *Phys. Rev. B* **57**, 5029 (1998).
  - [34] C. Gao (private communication)
  - [35] M. A. Ruderman and C. Kittel, *Phys. Rev.* **96**, 99 (1954).
  - [36] T. Kasuya, *Prog. Theor. Phys.* **16**, 45 (1956).
  - [37] K. Yosida, *Phys. Rev.* **106**, 893 (1957).
  - [38] S. S. P. Parkin and D. Mauri, *Phys. Rev. B* **44**, 7131 (1991).
  - [39] D. Šabani, C. Bacaksiz, and M. V. Milošević, *Phys. Rev. B* **102**, 014457 (2020).
  - [40] G. Kresse and J. Hafner, *Phys. Rev. B* **47**, 558 (1993).
  - [41] G. Kresse and J. Furthmüller, *Phys. Rev. B* **54**, 11169 (1996).

- [42] P. E. Blöchl, *Phys. Rev. B* **50**, 17953 (1994).
- [43] G. Kresse and D. Joubert, *Phys. Rev. B* **59**, 1758 (1999).
- [44] H. J. Monkhorst and J. D. Pack, *Phys. Rev. B* **13**, 5188 (1976).
- [45] W. Schäfer, G. Will, and K. H. J. Buschow, *J. Chem. Phys.* **64**, 1994 (1976).
- [46] L. Regeciová and P. Farkašovsky, *Eur. Phys. J. B* **93**, 110 (2020).
- [47] J. J. Feng, L. Huo, W. C. Huang, Y. Wang, M. H. Qin, J.-M. Liu, and Z. Ren, *Europhys. Lett.* **105**, 17009 (2014).
- [48] A. Ikeda and H. Kawamura, *J. Phys. Soc. Jpn.* **77**, 073707 (2008).
- [49] Q. Xu, Y. Liu, S. Hao, J. Qian, C. Su, C.-W. Wang, T. Hansen, Z. Fu, Y. Su, W. Li, G.-H. Cao, Y. Xiao, and W. Jin, *Phys. Rev. Res.* **4**, 013077 (2022).
- [50] A. D. Becke and K. E. Edgecombe, *J. Chem. Phys.* **92**, 5397 (1990).
- [51] B. Skubic, J. Hellsvik, L. Nordström, and O. Eriksson, *J. Phys.: Condens. Matter* **20**, 315203 (2008).
- [52] <https://www.physics.uu.se/en/page/UppASD>.